Design and multi-objective optimization of a novel 5-DOF parallel mechanism with two double-driven chains

Xuhao Wang [ID], Yufei Lin [ID], Yiran Cao, Mengli Wu [ID] and Shuo Sun

College of Aeronautical Engineering, Civil Aviation University of China, Tianjin 300300, China
Corresponding authors: Yiran Cao, Mengli Wu; Emails: yrcao@cauc.edu.cn, wuml2004@qq.com

Abstract

This paper focuses on the design, analysis, and multi-objective optimization of a novel 5-degrees of freedom (DOF) double-driven parallel mechanism. A novel 5-DOF parallel mechanism with two double-driven branch chains is proposed, which can serve as a machine tool. By installing two actuators on one branch chain, the proposed parallel mechanism can achieve 5-DOF of the moving platform with only three branch chains. Afterwards, analytical solution for inverse kinematics is derived. The 5×5 homogeneous Jacobian matrix is obtained by transforming actuator velocities into linear velocities at three points on the moving platform. Meanwhile, the workspace, dexterity, and volume are analyzed based on the kinematic model. Ultimately, a stage-by-stage Pareto optimization method is proposed to solve the multi-objective optimization problem of this parallel mechanism. The optimization results show that the workspace, compactness, and dexterity of this mechanism can be improved efficiently.

1. Introduction

The parallel mechanism typically consists of a moving platform, a fixed base, and at least two branch chains. It belongs to a kind of mechanism with multi-chain closed loops [1,2]. Parallel mechanism has a wide development prospection because of its strong load ability, high stiffness, and excellent dynamic performance [3]. Therefore, many scholars and enterprises have been committed to the design and research of parallel mechanisms with engineering application value [4].

The number of degrees of freedom (DOF) of traditional parallel mechanisms is usually the same as the number of branches with driving joints. In other words, the number of branches with driving joints determines the number of DOF of traditional parallel mechanisms [5]. However, when the parallel mechanism has more than 3-DOF, multiple branch chains will not only cause the mechanisms' complex structure but also lead to easy interference between branch chains [6]. In order to avoid a series of disadvantages of multi-branch parallel mechanisms, many scholars have carried out systematic research on the structural configuration. At present, hybrid mechanism, which is composed of parallel and series structures, is the mainstream idea to solve this kind of problem [7]. The number of DOF of hybrid mechanism is determined by series structure and parallel structure. The hybrid mechanism not only makes up for the shortage of working space of the pure parallel mechanism but also overcomes the low stiffness and cumulative error of the pure series mechanism [8]. The typical hybrid mechanism is represented by Trivaiant, Tricept and Exechon, etc. [9]. Nevertheless, due to the existence of serial structure, the end stiffness and positioning accuracy of hybrid mechanisms are not as good as that of the pure parallel mechanism.

Double-driven parallel mechanism [10] is an alternative to reduce the number of branch chains while ensuring the number of DOF. Different from the traditional parallel mechanism, the double-driven parallel mechanism contains one or more double-driven branch chains (i.e. there are two or more drives

on one branch chain). The double-driven parallel mechanism still belongs to the closed-loop structure, which retains the advantages of large stiffness and high positioning accuracy. The research on the double-driven parallel mechanism is still in its infancy, and there are few design cases. Lu *et al.* [11] proposed a three branch chain 5-DOF mechanism with two double-driven branch chains, namely the 2UPS-SPR dual-drive parallel mechanism, and proved that the single-branch multi-drive mechanism had the advantages of reducing vibration interference between branches, easy to avoid singularity, and high dexterity. Zhao *et al.* [12] proposed and studied a double-driven parallel mechanism with sub-closed loops, concluding that the double-driven parallel mechanism with sub-closed loop structure has strong posture adjustment and vibration isolation ability. Louis *et al.* [13] analyzed a double-driven parallel mechanism with three double-driven branch chains and three precisely constrained branch chains. This mechanism has three redundant DOFs, which can be used to avoid singulars and expand the rotating workspace, although above scholars have designed several double-driven mechanisms and verified that they have many advantages. Nevertheless, as a new research direction, considering that the structural strategy has a great influence on the performance of the whole mechanism, driving mode and the corresponding layout of double-driven chains are still open issues to be further studied [14].

Optimal design is an important research direction in parallel mechanism development [15]. Among, the kinematic design mainly involves the determination of optimal geometric parameters [16]. Establishing performance indexes [17] is the first step of kinematic multi-objective optimization. Workspace and dexterity of the mechanism are mainly used as the kinematic performance optimization indexes so far [18,19]. Considering compactness and economy of parallel mechanisms, the mechanism volume is also used as the performance index frequently. Wu *et al.* [20] used kinematic performance such as mechanism workspace and volume as optimization indexes for multi-objective optimization of a novel 6-DOF painting robot. Huang *et al.* [21] used the performance of workspace, stiffness, and dexterity as optimization indexes for multi-objective optimization to improve the overall performance of a reconfigurable parallel mechanism. In conclusion, this paper mainly carries out the kinematic multi-objective for the new proposed mechanism by using workspace, volume, and dexterity as performance indexes.

Multi-objective optimization mainly includes two aspects: optimization method and optimization algorithm [22]. As for the multi-objective optimization method, there are mainly two strategies [23]. The first method is to define the sum of the weights of multiple performance indexes as a comprehensive index (the sum of the weight factors is equal to 1), commonly called the comprehensive objective method [24]. The second method is known as the Pareto optimization method, which obtains non-dominated solution sets for multiple performance indexes [25]. The determination of weight factors in the comprehensive objective method is subjective and requires a large amount of computing time, so its optimization efficiency is low [26]. Because Pareto optimization is an after-the-fact decision, this method is usually given priority in multi-objective optimization [27]. The Pareto front is defined as the set of all optimal solutions produced by Pareto optimization. Solutions on the Pareto front are all equal and can be regarded as the optimal solution of Pareto optimization [28]. Russo *et al.* [29] designed a parallel mechanism with 3-UPR architecture based on the Pareto optimization method. The kinematic performance of this mechanism, such as workspace and manipulator dexterity, is improved. Qi *et al.* [30] used Pareto optimization to determine the optimal structural parameters of a novel parallel tracking mechanism. However, in the above studies, it is a challenge to select the optimal solution according to weight combinations in Pareto optimization. Generally, the performance graph that displays the relation between design variables and the performance can be used intuitively to select the final optimization result from the Pareto front [31]. And for the traditional Pareto optimization, Pareto front of the two optimization indexes can be drawn as a curve, which can be visually displayed on a two-dimensional plane. However, the Pareto front of three or more optimization indexes is a hypersurface, which cannot be visually displayed by two-dimensional graphics, thus increasing the difficulty in determining the final optimization results [32]. Therefore, it is very meaningful to improve the traditional Pareto optimization process so as to intuitively select the final optimization results and reduce the difficulty of optimization results selection. Finally, as for the optimization algorithm, the intelligence optimization algorithm,
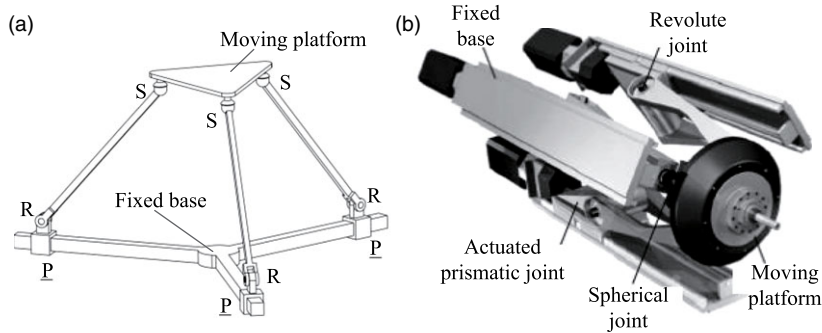
Figure 1. *The 3-PRS parallel mechanism. (a) Topology structure of 3-PRS parallel mechanism. (b) Sprint Z_3.*

such as genetic algorithm (GA) and particle swarm optimization (PSO) algorithm [33], is often used in a real-life engineering setting. The main disadvantage of GA is that many parameters need to be selected by experiences, such as the operator parameters of crossover rate and mutation rate [34]. Different from the crossover and mutation operating of GA, PSO is easier to be implemented because the search is determined according to its speed [35]. Yun *et al.* [36] found that fitness value of the PSO algorithm is better than that of the GA in the optimization of a 3PUPU parallel mechanism. Wang *et al.* [37] used the PSO algorithm to optimize the workspace, input coupling rate, natural frequency, and stiffness performance of a planar 3-DOF parallel mechanism. The efficiency of PSO algorithm is widely recognized. Therefore, the PSO algorithm is selected as the optimization algorithm in this paper.

In this paper, a novel 5-DOF parallel mechanism with two double-driven branch chains is proposed and analyzed based on the idea of double-driven. And the kinematic multi-objective optimization problem is systematically studied based on a novel stage-by-stage Pareto optimization method. The structure of this paper is as follows. Section 2 introduces design ideas of the proposed mechanism and carries out the DOF analysis. In Section 3, the kinematics problem is studied. The inverse kinematic solution and 5×5 dimensional Jacobian matrix are obtained. Section 4 analyzes the kinematic performance of the proposed mechanism. In Section 5, a stage-by-stage Pareto optimization method is proposed to perform multi-objective optimization of the parallel mechanism. Conclusions are drawn in Section 6.

2. Design and DOF analysis of the parallel mechanism

2.1. Mechanism design

Based on the idea of double-driven, this paper is devoted to designing a double-driven parallel structure with 5-DOF. The parallel mechanism with three branch chains, especially 3-PRS [38] (P denotes actuated prismatic joint, R denotes revolute joint, S denotes spherical joint) parallel mechanism, is usually used as the base mechanism for designing double-driven parallel mechanism because of its simple structure and high stability, etc.

The topology structure of the 3-PRS parallel mechanism is shown in Fig. 1(a). The 3-PRS parallel mechanism has three PRS branch chains of the same structure. Two ends of the three branches are connected with the moving platform and fixed base, respectively. At present, the 3-PRS parallel mechanism has been widely used in the field of machine tool processing, such as Sprint Z_3 [39] shown in Fig. 1(b).

Inspired by the idea of double-driven, a novel 5-DOF parallel mechanism is designed based on the 3-PRS parallel mechanism, shown in Fig. 2(a). As the main improvement, an additional actuated revolute joint (i.e. R) is added to two branch chains of the 3-PRS parallel mechanism, respectively. And, the third PRS branch chain is replaced with a PUU branch chain to meet the movement requirements of the mechanism. Here, U represents universal joint. As a result, the proposed PUU-2PRRS parallel mechanism can realize 5-DOF of moving platform with only three branch chains. However, the structure uses rotationally driven double-driven branch chains, resulting in a load close to the moving platform.
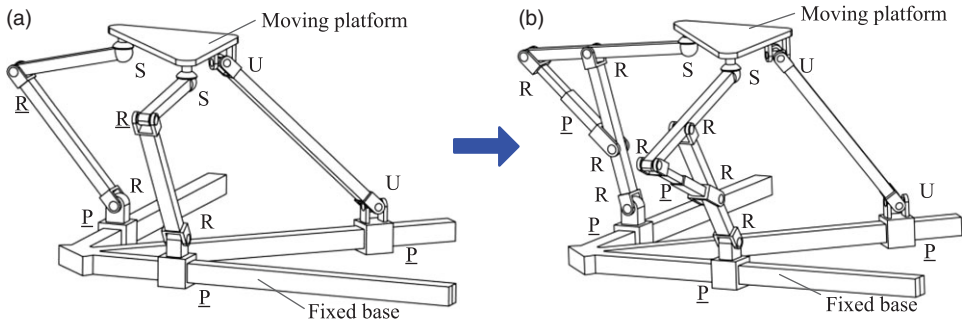
Figure 2. *Novel double-driven parallel mechanism. (a) $\underline{P}$UU-2$\underline{P}$RRS parallel mechanism. (b) $\underline{P}$UU-2$\underline{P}$R($\underline{R}$PRR)S parallel mechanism.*
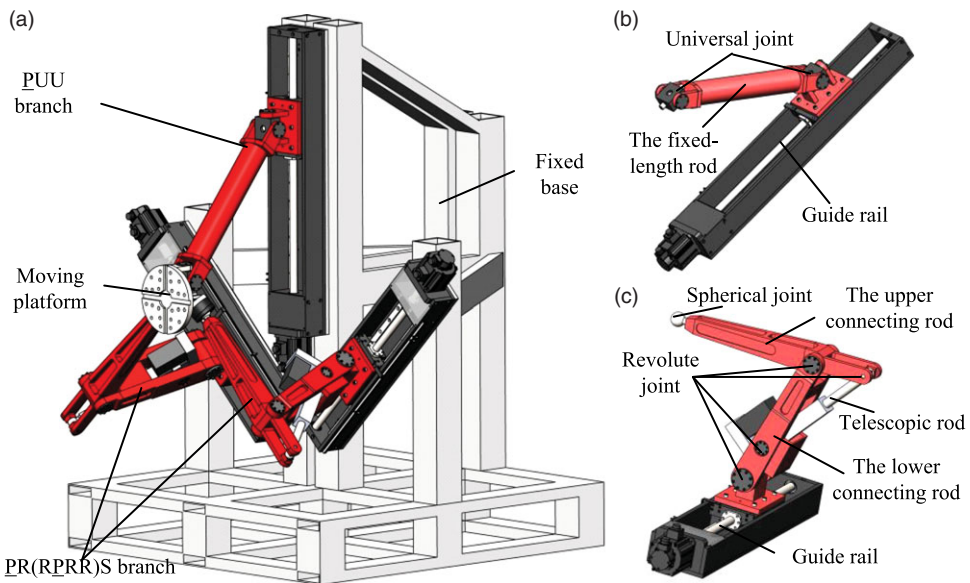

Figure 3. *3D model of the $\underline{P}$UU-2$\underline{P}$R($\underline{R}$PRR)S parallel mechanism. (a) The $\underline{P}$UU-2$\underline{P}$R($\underline{R}$PRR)S parallel mechanism. (b) $\underline{P}$UU branch chain. (c) Double-driven branch chain.*

The layout of the drive motor of the parallel mechanism has an important influence on its overall performance. Generally speaking, the drive motor close to the fixed base can ensure the maximum stiffness. Therefore, the $\underline{P}$UU-2$\underline{P}$RRS parallel mechanism needs to be improved.

It is notable that the actuated revolute pair on the double-driven branch chains would cause large deformation and great difficulty in control. To solve this problem, the $\underline{P}$UU-2$\underline{P}$R($\underline{R}$PRR)S parallel mechanism with sub-closed-loop is designed. The actuated revolute joint is designed as a sub-closed-loop (i.e. $\underline{R}$PRR). The sub-closed-loop changes the rotation drive to a linear drive. By introducing the sub-closed-loop structure, drive the motor and other loads near the fixed base. What is more, the vibration, manufacturing costs, and control difficulty of the mechanism can be reduced effectively. Finally, the topology of the $\underline{P}$UU-2$\underline{P}$R($\underline{R}$PRR)S parallel mechanism is shown in Fig. 2(b). According to the topological structure of Fig. 2(b), the 3D model structure of this mechanism is designed. As shown in Fig. 3(a), a $\underline{P}$UU branch chain and two double-driven branch chains connect the moving platform to the fixed base in the $\underline{P}$UU-2$\underline{P}$R($\underline{R}$PRR)S parallel mechanism. Figure 3(b) shows the structure of the PUU branch chain. $\underline{P}$UU branch consists of a guide rail and a fixed-length rod which are connected by a universal joint. Figure 3(c) shows the structure of the double-driven branch chain (i.e. $\underline{P}$R($\underline{R}$PRR)S branch chain).

Table I. *Structure parameters of the PUU-2PR(RPRR)S parallel mechanism.*

| Structure parameters	Meaning
l_1 (mm)	Distance from point B_1 to point C_1
l_2 (mm)	Distance from point C_{i+1} to point $D_i (i = 1, 2)$
l_3 (mm)	Distance from point B_{i+1} to point $D_i (i = 1, 2)$
l_4 (mm)	Distance from point D_i to point $F_i (i = 1, 2)$
l_5 (mm)	Distance from point D_i to point $E_i (i = 1, 2)$
b (mm)	Distance from point B_1 to point B_4
g_i (mm)	Distance from point O_1 to point $C_i (i = 1, 2, 3)$ or the distance from point E_{i-3} to point $F_{i-3} (i = 4, 5)$
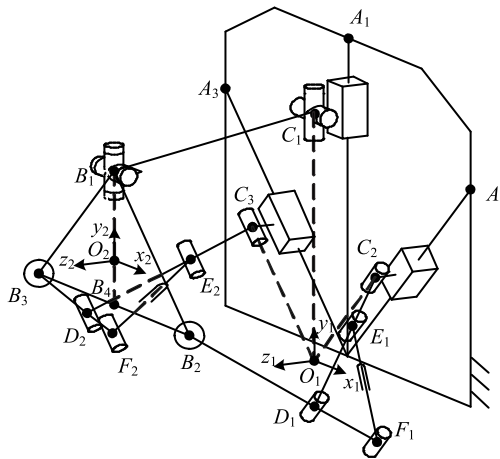
Figure 4. *Simplified schematic diagram of the PUU-2PR(RPRR)S parallel mechanism.*

PR(RPRR)S branch consists of a guide rail, the lower connecting rod, and the upper connecting rod which are in turn connected by two revolute joints. The connection between the upper connecting rod and the lower connecting rod also adopts a telescopic rod-driven sub-closed-loop rotation component (i.e. RPRR).

All three chain guides are mounted on the same plane of the fixed base. The guide rails of the two double-driven branch chains are perpendicular to each other.

In order to facilitate the study of the PUU-2PR(RPRR)S parallel mechanism, its mechanism schematic structure is established as shown in Fig. 4. O_1 is taken as the origin to set up the fixed Cartesian coordinate system $O_1 - x_1y_1z_1$. It is the intersection point of three linear guides on the plane $C_1C_2C_3$. z_1-axis is perpendicular to the base guide rail installation plane, y_1-axis is in the same direction as $\overline{O_1C_1}$, and x_1-axis satisfies the right-hand rule. The structure parameters of the PUU-2PR(RPRR)S parallel mechanism are shown in Table I.

O_2 is taken as the origin to set up the moving Cartesian coordinate system $O_2 - x_2y_2z_2$. It is the geometric center of the isosceles right triangle $\triangle B_1B_2B_3$. x_2-axis is in the same direction as $\overline{B_3B_2}$, y_2-axis is in the same direction as $\overline{O_2B_1}$, and z_2-axis satisfies the right-hand rule.

2.2. DOF of the PUU-2PR(RPRR)S parallel mechanism

Screw theory is the main method to calculate the DOF of parallel mechanisms [40]. As shown in Fig. 5, the local coordinate system $C_1 - x_{11}y_{11}z_{11}$ is established in the PUU branch chain. x_{11}-axis and y_{11}-axis are in the same direction as the two axes of universal joint, respectively.
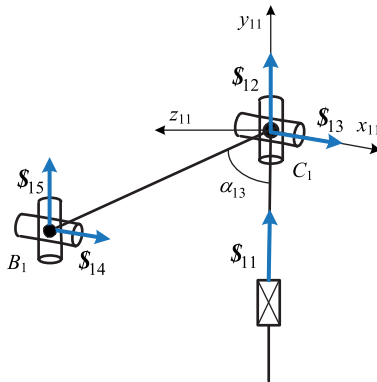
Figure 5. *Sketch of the PUU branch chain.*

R_{O1}^{C1} is the transformation matrix from $O_1 - x_1y_1z_1$ to $C_1 - x_{11}y_{11}z_{11}$. It can be expressed as

$$R_{O1}^{C1} = \begin{bmatrix} c\beta_{12} & 0 & s\beta_{12} \\ 0 & 1 & 0 \\ -s\beta_{12} & 0 & c\beta_{12} \end{bmatrix} \tag{1}$$

where s denote sine and c denote cosine. β_{12} is the angle between x_{11}-axis and x_1-axis.

The coordinates of B_1 in $C_1 - x_{11}y_{11}z_{11}$ can be denoted as

$$B_1^{C1} = (0 \quad -l_1c\alpha_{13} \quad l_1s\alpha_{13})^T \tag{2}$$

where α_{13} is the angle between $\overline{C_1B_1}$ and $\overline{C_1O_1}$.

The kinematic screw system of the PUU branch chain in $C_1 - x_{11}y_{11}z_{11}$ can be expressed as

$$\$_1 = \begin{cases} \$_{11} = (O_{3\times1}; e_2) = (0\ 0\ 0\ ; 0\ 1\ 0)^T \\ \$_{12} = (e_2; O_{3\times1}) = (0\ 1\ 0\ ; 0\ 0\ 0)^T \\ \$_{13} = (e_1; O_{3\times1}) = (1\ 0\ 0\ ; 0\ 0\ 0)^T \\ \$_{14} = (e_1; \overline{C_1B_1^{C1}} \times e_1) = (1\ 0\ 0\ ; 0\ l_1s\alpha_{13}\ l_1c\alpha_{13})^T \\ \$_{15} = (s_{15}; \overline{C_1B_1^{C1}} \times s_{15}) = (0\ c\theta_{25}\ s\theta_{25}\ ; -l_1(c\alpha_{13}s\theta_{25} + s\alpha_{13}c\theta_{25})\ 0\ 0)^T \end{cases} \tag{3}$$

where $e_1 = [1\ 0\ 0]^T$, $e_2 = [0\ 1\ 0]^T$, $O_{3\times1} = [0\ 0\ 0]^T$, $\overline{C_1B_1^{C1}} = B_1^{C1}$. $s_{15} = [0\ c\theta_{25}\ s\theta_{25}]^T$ is the unit vector along $\$_{15}$, and θ_{25} is the angle between y_{11}-axis and s_{15}.

Based on the reciprocity between screw systems, the reciprocal screw system of the PUU branch chain can be expressed as

$$\$_1^r = (s\theta_{25} \quad 0 \quad 0 \quad 0 \quad 0 \quad L_1)^T \tag{4}$$

where $L_1 = l_1(c\alpha_{13}s\theta_{25} + s\alpha_{13}c\theta_{25})$.

Similarly, the screw theory is used to prove that two double-driven branch chains have no constraints.

The reciprocal screw system of Eq. (4) needs to be converted to the fixed Cartesian coordinate system $O_1 - x_1y_1z_1$. It can be calculated by

$$\$^r = \begin{bmatrix} R_{O1}^{C1} & O_{3\times3} \\ [\overline{O_1C_1}\times] R_{O1}^{C1} & R_{O1}^{C1} \end{bmatrix} \cdot \$_1^r \tag{5}$$

where $[\overline{O_1C_1}\times] = \begin{bmatrix} 0 & 0 & g_1 \\ 0 & 0 & 0 \\ -g_1 & 0 & 0 \end{bmatrix}$.

Submitting Eqs. (1) and (4) into Eq. (5), $\$^r$ can be represented as

$$\$^r = \begin{pmatrix} s\theta_{25}c\beta_{12} & 0 & -s\theta_{25}s\beta_{12} & (L_1 - s\theta_{25}g_1)s\beta_{12} & 0 & (L_1 - s\theta_{25}g_1)c\beta_{12} \end{pmatrix}^T \tag{6}$$

From Eq. (6), the $\underline{P}$UU-2$\underline{P}$R(R$\underline{P}$RR)S parallel mechanism has only one constraint. In other words, the $\underline{P}$UU-2$\underline{P}$R(R$\underline{P}$RR)S parallel mechanism has 5-DOF. Additionally, in $O_1 - x_1y_1z_1$, $\$^r$ is a spiral rather than pure rotation or line displacement. So the $\underline{P}$UU-2$\underline{P}$R(R$\underline{P}$RR)S parallel mechanism has a parasitic motion [41] in the generalized coordinate system.

The correctness of the result is judged by the modified Grübler–Kutzbach formula. The DOF of the parallel mechanism can be calculated as

$$N = d(n_0 - g - 1) + \sum_{k=1}^{g} f_k + v_0 - \xi = 6 \times (10 - 11 - 1) + 17 + 0 - 0 = 5 \tag{7}$$

where N is the number of DOF, d represents the space dimensionality, n_0 is the number of components, g is the number of various hinges, f_k means the number of DOF for the k-th motion pair, v_0 is the number of redundant constraints, and ξ is the number of local DOF.

3. Kinematics of the parallel mechanism

3.1. Parasitic motion analysis

For the limited DOF parallel mechanism (i.e. the number of DOF is less than 6), motions in the desired DOF directions generally would generate constrained motions in the remaining directions (i.e. parasitic motion). From Section 2.2, the $\underline{P}$UU-2$\underline{P}$R(R$\underline{P}$RR)S parallel mechanism has a parasitic motion. In order to obtain the inverse kinematic solution, it is necessary to analyze this parasitic motion thoroughly.

The orientation of $O_2 - x_2y_2z_2$ with respect to $O_1 - x_1y_1z_1$ is expressed by XYZ Euler angle, (α β γ). It can be expressed as

$$\boldsymbol{R} = \text{Rot}(x, \alpha) \cdot \text{Rot}(y', \beta) \cdot \text{Rot}(z'', \gamma) = \begin{bmatrix} c\beta c\gamma & -c\beta s\gamma & s\beta \\ c\alpha s\gamma + s\alpha s\beta c\gamma & c\alpha c\gamma - s\alpha s\beta s\gamma & -c\beta s\alpha \\ s\alpha s\gamma - c\alpha s\beta c\gamma & s\alpha c\gamma + c\alpha s\beta s\gamma & c\alpha c\beta \end{bmatrix} \tag{8}$$

where $\boldsymbol{R}$ is the corresponding transformation matrix from $O_1 - x_1y_1z_1$ to $O_2 - x_2y_2z_2$.

The coordinates of point O_2 in $O_1 - x_1y_1z_1$ are expressed as

$$\boldsymbol{O}_2 = (x \ y \ z)^T \tag{9}$$

The position coordinates of point $C_i(i=1, 2, 3)$ in $O_1 - x_1y_1z_1$ can be expressed as

$$\boldsymbol{C}_1 = (0 \quad g_1 \quad 0)^T, \boldsymbol{C}_2 = \left(\frac{\sqrt{2}}{2}g_2 \quad \frac{\sqrt{2}}{2}g_2 \quad 0 \right)^T, \boldsymbol{C}_3 = \left(-\frac{\sqrt{2}}{2}g_3 \quad \frac{\sqrt{2}}{2}g_3 \quad 0 \right)^T \tag{10}$$

The position coordinates of point $B_i(i=1, 2, 3, 4)$ on the moving platform in $O_2 - x_2y_2z_2$ can be expressed as

$$\boldsymbol{B}_1^{O2} = \left(0 \quad \frac{2b}{3} \quad 0 \right)^T, \boldsymbol{B}_2^{O2} = \left(b \quad -\frac{b}{3} \quad 0 \right)^T \boldsymbol{B}_3^{O2} = \left(-b \quad -\frac{b}{3} \quad 0 \right)^T, \boldsymbol{B}_4^{O2} = \left(0 \quad -\frac{b}{3} \quad 0 \right)^T \tag{11}$$

Using the coordinate transformation approach, the position coordinates of point $B_i(i=1, 2, 3, 4)$ in $O_1 - x_1y_1z_1$ can be expressed as

$$\boldsymbol{B}_i = \boldsymbol{O}_2 + \boldsymbol{R}\boldsymbol{B}_i^{O2}(i=1, 2, \cdots, 4) \tag{12}$$

Because the fixed-length rod in the $\underline{P}$UU branch chain is connected by two universal joints, the guide axis $\boldsymbol{e}_2$ of the PUU branch chain and the center line O_2B_1 of the moving platform are coplanar

with the fixed-length rod. Submitting Eqs. (9), (10), and (12), then this geometric relationship can be expressed as

$$x \sin \alpha + (z \cos \beta + x \sin \beta \cos \alpha) \tan \gamma = 0 \tag{13}$$

After the simplification of Eq. (13), the analytical form of γ can be expressed as

$$\gamma = \arctan \left(\frac{-x \sin \alpha}{z \cos \beta + x \sin \beta \cos \alpha} \right) \tag{14}$$

It can be obtained from Eq. (14) that the P̱UU-2P̱R(RP̱RR)S parallel mechanism has five independent DOFs (i.e. x, y, z, α, and β). γ is the parasitic motion of the P̱UU-2P̱R(RP̱RR)S parallel mechanism.

3.2. Inverse kinematics

Inverse kinematic problem (IKP) [42] is the premise for kinematic performance analysis and motion control of the parallel mechanism. The IKP of the P̱UU-2P̱R(RP̱RR)S parallel mechanism is defined as follows: when the position and orientation of the moving platform (i.e. x, y, z, α, and β) are known, solve the actuator parameters (i.e. g_1, g_2, g_3, g_4 and g_5).

According to the geometric relations shown in Fig. 4, the following equation can be obtained as:

$$\left| \overline{B_1 C_1} \right| = \left| \overline{O_1 C_1} - \overline{O_1 B_1} \right| \tag{15}$$

Submitting Eqs. (10) and (12) into Eq. (15), g_1 can be expressed as

$$g_1 = y + \frac{2b}{3} (c\alpha c\gamma - s\alpha s\beta s\gamma) + \sqrt{ {l_1}^2 - \left(x - \frac{2b}{3} c\beta s\gamma \right)^2 - \left(z + \frac{2b}{3} (s\alpha c\gamma + c\alpha s\beta s\gamma) \right)^2 } \tag{16}$$

$\overline{B_i C_i}$ and $\overline{O_1 C_i}(i = 2, 3)$ are perpendicular to each other. This geometric relationship can be expressed as

$$\overline{B_i C_i} \cdot \overline{O_1 C_i} = 0 (i = 2, 3) \tag{17}$$

Submitting Eqs. (10) and (12) into Eq. (17), g_2 and g_3 can be represented as

$$\begin{cases} g_2 = \frac{\sqrt{2}}{2} \left(x + y + b (s\alpha s\beta c\gamma + c\alpha s\gamma + c\beta c\gamma) - \frac{b}{3} (c\alpha c\gamma - s\alpha s\beta s\gamma - c\beta s\gamma) \right) \\ g_3 = \frac{\sqrt{2}}{2} \left(-x + y - b (c\alpha s\gamma + s\alpha s\beta c\gamma - c\beta c\gamma) - \frac{b}{3} (c\alpha c\gamma + c\beta s\gamma - s\alpha s\beta s\gamma) \right) \end{cases} \tag{18}$$

Similarly, as shown in Fig. 6, the geometric relations for the PR(RPRR)S branch chain can be written as

$$\left| \overline{E_i F_i} \right|^2 = \left| \overline{D_i E_i} \right|^2 + \left| \overline{D_i F_i} \right|^2 - 2 \left| \overline{D_i E_i} \right| \cdot \left| \overline{D_i F_i} \right| \cdot \cos \phi_i (i = 1, 2) \tag{19}$$

where $\phi_i = \pi - \arccos \left(\frac{ {l_2}^2 + {l_3}^2 - \left| \overline{B_{i-1} C_{i-1}} \right|^2 }{2 l_2 l_3} \right)$ is the angle between $\overline{D_i E_i}$ and $\overline{D_i F_i}$ ($i = 1, 2$).

Submitting the data in Table I into Eq. (19), g_4 and g_5 can be represented as

$$\begin{cases} g_4 = \sqrt{ {l_4}^2 + {l_5}^2 - 2 l_4 l_5 \cos \phi_1 } \\ g_5 = \sqrt{ {l_4}^2 + {l_5}^2 - 2 l_4 l_5 \cos \phi_2 } \end{cases} \tag{20}$$

3.3. Homogeneous dimension Jacobin matrix

Jacobian matrix represents the relationship between the end-effector velocity and the drive speeds, which is the key to the kinematic performance analysis. Its condition number is often used to analyze the dexterity of the mechanism. However, if the mechanism has both translational and rotational DOF, the
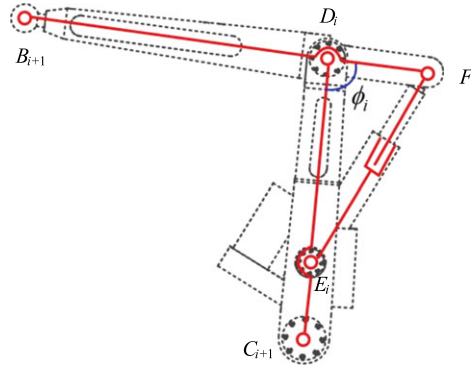
Figure 6. *Partial sketch of the P̲R(RP̲RR)S branch chain.*

velocity dimension of the moving platform is inconsistent, and its Jacobian matrix has non-homogeneous physical units, which leads to significant problem in which the computation of the condition number will vary with the scaling of dimensions [43,44]. To solve this problem, the Jacobian matrix needs to be normalized, and the dimensionally homogeneous Jacobian matrix could be derived by transforming actuator velocities into linear velocities of points on the moving platform [45]. Here, the key to establishing 5×5 dimensionally homogeneous dimensional Jacobian matrix of the P̲UU-2P̲R(RP̲RR)S parallel mechanism is to find five independent linear velocity components of three non-collinear points on the moving platform to replace the six-dimensional velocity vector of the moving platform.

Firstly, by taking the time derivative of Eqs. (16), (18), and (20), the following equation can be obtained:

$$\dot{G} = J_1 \dot{q} \tag{21}$$

where $\dot{G} = \begin{bmatrix} \dot{g}_1 & \dot{g}_2 & \dot{g}_3 & \dot{g}_4 & \dot{g}_5 \end{bmatrix}^{\mathrm{T}}$ means the vector composed of five linear driving velocities, $\dot{q} = \begin{bmatrix} \dot{x} & \dot{y} & \dot{z} & \dot{\alpha} & \dot{\beta} & \dot{\gamma} \end{bmatrix}^{\mathrm{T}}$ is the six-dimensional velocity vector of the moving platform, J_1 is denoted as the inverse Jacobian matrix, and it can be expressed as

$$J_1 = \begin{bmatrix} \dfrac{\partial g_1}{\partial x} & \dfrac{\partial g_1}{\partial y} & \dfrac{\partial g_1}{\partial z} & \dfrac{\partial g_1}{\partial \alpha} & \dfrac{\partial g_1}{\partial \beta} & \dfrac{\partial g_1}{\partial \gamma} \\ \dfrac{\partial g_2}{\partial x} & \dfrac{\partial g_2}{\partial y} & \dfrac{\partial g_2}{\partial z} & \dfrac{\partial g_2}{\partial \alpha} & \dfrac{\partial g_2}{\partial \beta} & \dfrac{\partial g_2}{\partial \gamma} \\ \cdots & \cdots & \cdots & \cdots & \cdots & \cdots \\ \dfrac{\partial g_5}{\partial x} & \dfrac{\partial g_5}{\partial y} & \dfrac{\partial g_5}{\partial z} & \dfrac{\partial g_5}{\partial \alpha} & \dfrac{\partial g_5}{\partial \beta} & \dfrac{\partial g_5}{\partial \gamma} \end{bmatrix}_{5 \times 6} \tag{22}$$

Secondly, the velocity vector of the moving platform can be expressed as

$$\dot{q} = J_2 \cdot \dot{q}_{o2} \tag{23}$$

where $\dot{q}_{o2} = \begin{bmatrix} v'_{o2} & \omega'_{o2} \end{bmatrix}^{\mathrm{T}}$, v'_{o2} and ω'_{o2} represent the representation of $\begin{bmatrix} \dot{x} & \dot{y} & \dot{z} \end{bmatrix}^{\mathrm{T}}$ and $\begin{bmatrix} \dot{\alpha} & \dot{\beta} & \dot{\gamma} \end{bmatrix}^{\mathrm{T}}$ in $O_2 - x_2 y_2 z_2$, respectively. $J_2 = \begin{bmatrix} R & O_{3\times 3} \\ O_{3\times 3} & R \end{bmatrix}_{6\times 6}$ is the velocity transformation matrix from $O_1 - x_1 y_1 z_1$ to $O_2 - x_2 y_2 z_2$.

Thirdly, the mapping between the six-dimensional velocity vector of B_1 in $B_1 - x_3 y_3 z_3$ and the six-dimensional velocity vector of O_2 in $O_2 - x_2 y_2 z_2$ needs to be established. Here, $B_1 - x_3 y_3 z_3$ is set at point B_1. It has the same axis direction as $O_2 - x_2 y_2 z_2$.

The relationship between the linear velocities of B_1 and O_2 can be expressed as

$$v_{B1} = v'_{O2} + \omega'_{O2} \times \overline{O_2 B_1} \; , \; v'_{O2} = v_{B1} + \omega_{B1} \times \overline{B_1 O_2} \tag{24}$$

where $v_{B1} = \begin{bmatrix} v_{B1x} & v_{B1y} & v_{B1z} \end{bmatrix}^{\mathrm{T}}$, $\omega_{B1} = \begin{bmatrix} \omega_{B1x} & \omega_{B1y} & \omega_{B1z} \end{bmatrix}^{\mathrm{T}}$. v_{Bix}, v_{Biy}, v_{Biz}, ω_{Bix}, ω_{Biy} and ω_{Biz} are the linear velocity of B_i ($i = 1, 2, 3$) along x_3, y_3, z_3 and the angular velocity around x_3, y_3, z_3, respectively.

Combining Eq. (24), the mapping matrix between the six-dimensional velocity vector of B_1 in $B_1 - x_3 y_3 z_3$ and the six-dimensional velocity vector of O_2 in $O_2 - x_2 y_2 z_2$ can be denoted as

$$\begin{bmatrix} v_{B1} \\ \omega_{B1} \end{bmatrix} = J_3 \cdot \begin{bmatrix} v'_{O2} \\ \omega'_{O2} \end{bmatrix} \tag{25}$$

where $J_3 = \begin{bmatrix} E_3 & J_3^1 \\ O_{3\times3} & E_3 \end{bmatrix}_{6\times6}$, $E_3 = \begin{bmatrix} 1 & 0 & 0 \\ 0 & 1 & 0 \\ 0 & 0 & 1 \end{bmatrix}$, $J_3^1 = \begin{bmatrix} 0 & 0 & -\frac{2b}{3} \\ 0 & 0 & 0 \\ \frac{2b}{3} & 0 & 0 \end{bmatrix}$.

Fourthly, the mapping matrix between the velocity vector of B_i ($i = 1, 2, 3$) in $B_1 - x_3 y_3 z_3$ and the six-dimensional velocity vector of B_1 in $B_1 - x_3 y_3 z_3$ needs to be established. According to the rigid body motion relation,

$$v_{B2} = v_{B1} + \omega_{B1} \times \overline{B_1 B_2} \; , \; v_{B3} = v_{B1} + \omega_{B1} \times \overline{B_1 B_3} \tag{26}$$

where $v_{B2} = \begin{bmatrix} v_{B2x} & v_{B2y} & v_{B2z} \end{bmatrix}^{\mathrm{T}}$, $v_{B3} = \begin{bmatrix} v_{B3x} & v_{B3y} & v_{B3z} \end{bmatrix}^{\mathrm{T}}$.

The following expression can be obtained by associating Eq. (26):

$$\begin{bmatrix} v_{B1} \\ v_{B2} \\ v_{B3} \end{bmatrix}_{9\times1} = \begin{bmatrix} E_3 & O_{3\times3} \\ E_3 & J_4^1 \\ E_3 & J_4^2 \end{bmatrix}_{9\times6} \cdot \begin{bmatrix} v_{B1} \\ \omega_{B1} \end{bmatrix}_{6\times1} \tag{27}$$

where $J_4^1 = \begin{bmatrix} 0 & 0 & b \\ 0 & 0 & b \\ -b & -b & 0 \end{bmatrix}$, $J_4^2 = \begin{bmatrix} 0 & 0 & b \\ 0 & 0 & -b \\ -b & b & 0 \end{bmatrix}$.

According to the DOF analysis in Section 2.2, the moving platform cannot rotate around z_3, which means that $\omega_{B1z} = 0$. Then Eq. (27) can be reduced to

$$J_4 \cdot v = \begin{bmatrix} v_{B1} \\ \omega_{B1} \end{bmatrix} \tag{28}$$

where $J_4 = \begin{bmatrix} E_{5\times5} \\ 0_{1\times5} \end{bmatrix}_{6\times5} \cdot \begin{bmatrix} 0 & 0 & 1 & 0 & 0 \\ 1 & 0 & 0 & 0 & 0 \\ 0 & 0 & 1 & -b & -b \\ 0 & 1 & 0 & 0 & 0 \\ 0 & 0 & 1 & -b & b \end{bmatrix}_{5\times5}^{-1}$, $v = \begin{bmatrix} v_{B1z} & v_{B2x} & v_{B2z} & v_{B3y} & v_{B3z} \end{bmatrix}^{\mathrm{T}}$.

Finally, combining Eqs. (21), (23), (25), and (28), a 5×5 homogeneous Jacobian matrix of the $\underline{P}UU$-$2\underline{P}R(R\underline{P}RR)S$ parallel mechanism can be derived as

$$J \cdot v = \dot{G} \tag{29}$$
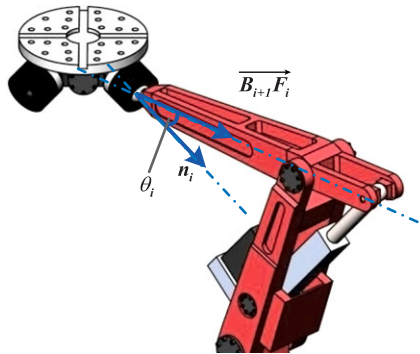
where $J = J_1 J_2 J_3^{-1} J_4$.

Figure 7. *Schematic diagram of rotation angle of spherical joint.*

4. Performance analysis

Based on the above IKP and Jacobian matrix, the kinematic performance of the proposed mechanism can be analyzed. This section mainly analyzes the workspace, mechanism volume, and dexterity of the PUU-2PR(RPRR)S parallel mechanism.

4.1. Workspace

Workspace is a collection of points that the moving platform can reach under the constraints of rod length, joint rotation angle, and interference. The workspace size is one of the most important indexes of parallel mechanisms. The numerical discrete method [46] is a commonly used method for parallel mechanism workspace analysis.

The PUU-2PR(RPRR)S parallel mechanism has 5-DOF. Using the numerical discrete method, the workspace solving problem of this mechanism can be converted to solving the position workspace with a constant posture. The posture space range of the moving platform is given by its design requirements, that is, $-10° \leq \alpha, \beta \leq 10°$.

The stroke of driving joints is one of the factors that determine the workspace size. Because the five driving joints of this mechanism are all linear moving actuators, the travel limit of five driving joints is composed of the maximum and minimum values that they can reach. The constraints of each driving joint can be expressed as

$$g_{i\min} \leq g_i \leq g_{i\max} \ (i = 1, 2, \cdots, 5) \tag{30}$$

where $g_{i\max}$ and $g_{i\min}$, respectively, represent the maximum and minimum limit length that can be reached by the i-th linear actuator.

Additionally, the rotation angle of spherical joint will affect the working space of this mechanism. As shown in Fig. 7, the rotation angle of spherical joint (i.e. θ_i) can be represented by the angle between the normal direction of spherical joint support and axis direction (i.e. $\overline{B_{i+1}F_i}$) of the upper connecting rod. θ_i can be denoted as

$$\theta_i = \arccos \frac{n_i \cdot \overline{B_{i+1}F_i}}{\left| \overline{B_{i+1}F_i} \right|} (i = 1, 2) \tag{31}$$

where n_i is the unit normal direction vector of the spherical joint support.

In order to avoid interference between each component, the constraint angle of spherical joint is given by

$$0 \leq \theta_i \leq \theta_{\max} \ (i = 1, 2) \tag{32}$$

where $\theta_{\max}$ is the maximum limit rotation angle of the spherical joint.
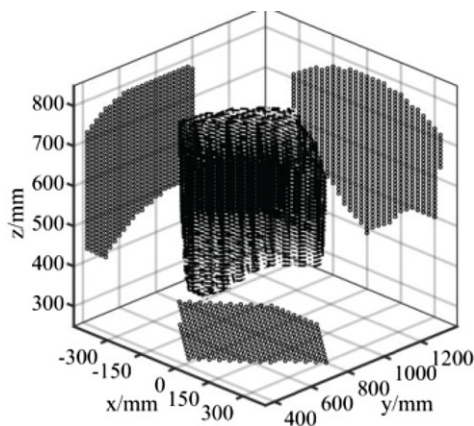
Figure 8. *Workspace of the PUU-2PR(RPRR)S parallel mechanism.*

On the premise of meeting the above constraints, the workspace of this mechanism is shown in Fig. 8. The workspace of the mentioned mechanism is continuous. And the shape is approximately a regular cylinder. The projection of the working space on the three projection planes shows that this mechanism has a certain range of motion in all directions.

4.2. Dexterity

The dexterity index is another important index to evaluate the kinematic performance of parallel mechanisms. After establishing the homogeneous dimensional Jacobian matrix, the dexterity index can be expressed as the reciprocal of Jacobian matrix' condition number.

$$\kappa = \frac{\sigma_{\min}}{\sigma_{\max}} \tag{33}$$

where $\sigma_{\min}$ and $\sigma_{\max}$, respectively, represent the minimum singular value and the maximum singular value of $\boldsymbol{J}$.

Obviously, from Eq. (33), $0 \leq \kappa \leq 1$. The larger the κ is, the better the transmission performance is. On the contrary, when $\kappa = 0$, the mechanism will be in a singular position and the transmission performance is the worst.

As shown in Fig. 9(a), it is the distribution of dexterity in the position workspace, when the moving platform is at a constant posture (i.e. $\alpha = 0°$ and $\beta = 0°$). From Fig. 9(a), the highest dexterity appears at the center point of the workspace, that is, $\boldsymbol{O}_2^{\mathrm{dM}} = (0\ 750\ 650)^{\mathrm{T}}$. The closer the distance to the edge of the workspace, the worse the dexterity is. To further analyze the influence of posture, Fig. 9(b) shows the distribution map of dexterity in the posture workspace, when the moving platform is at a constant position, that is, $\boldsymbol{O}_2^{\mathrm{dM}}$. The dotted box is the required posture of this mechanism. It can be seen that the posture space of this mechanism is roughly located in the area with excellent dexterity.

4.3. Mechanism volume

Mechanism volume refers to the space occupied by the mechanism, which is directly determined by the structure layout and structure size of the mechanism [47]. Mechanism volume directly affects the size of the mechanism station. Under the same working conditions, the smaller the size of mechanisms, the smaller the station reserved for mechanisms in the workshop. The energy consumption for workshop cleaning and temperature control can be also reduced to ensure the economy of the mechanism.
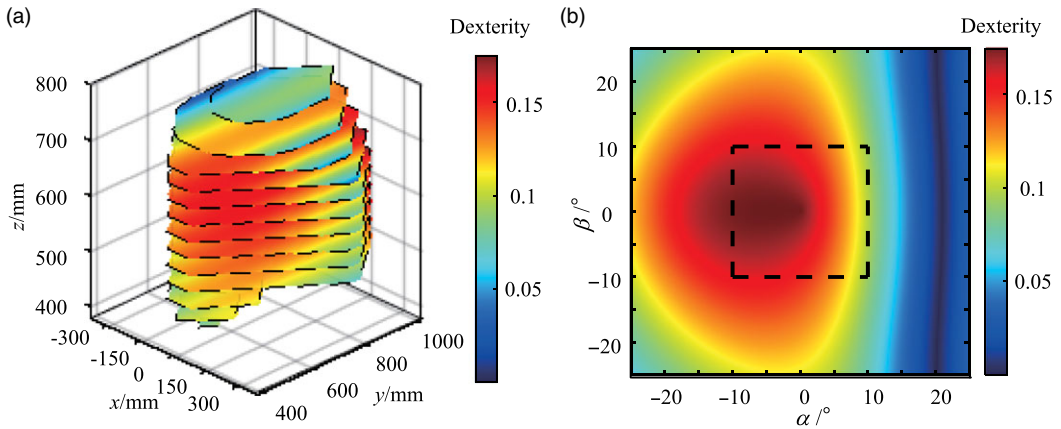
Figure 9. *Distribution map of the dexterity in workspace. (a) The distribution map of dexterity in position workspace. (b) The distribution map of dexterity in posture workspace.*
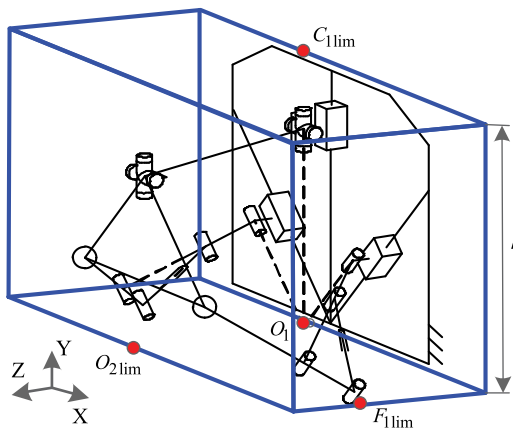

Figure 10. *Schematic diagram of the mechanism volume.*

Mechanism volume is positively correlated with the size and number of branch chains [48]. Due to the adoption of double-driven branch chains, the proposed mechanism reduces two branch chains compared with the traditional 5-DOF mechanism, reducing mechanism volume.

Generally, mechanism volume can be defined as a cube volume, as shown in Fig. 10. The boundary of the cube can be calculated from the limiting positions of O_2, F_1, C_1 (i.e. $O_{2\,\text{lim}}$, $F_{1\,\text{lim}}$ and $C_{1\,\text{lim}}$) and O_1 in the fixed coordinate system. The calculation formula is

$$V_{\text{m}} = h \cdot \max\{O_{2z}\} \cdot 2 \max\{F_{1x}\} \tag{34}$$

where $h = \max\{g_1\}$ represents the height of the mechanism volume, $\max\{g_1\}$ is the distance from $C_{1\,\text{lim}}$ to O_1, $\max\{O_{2z}\}$ is the coordinate of $O_{2\,\text{lim}}$ on the z_1-axis, and $\max\{F_{1x}\}$ represents the coordinate of $F_{1\,\text{lim}}$ on the x_1-axis.

5. Multi-objective optimization designs

In order to make the proposed mechanism more suitable for practical engineering, it is necessary to optimize the structural parameters to exert its best performance. In this section, a stage-by-stage

Pareto optimization method is proposed to conduct multi-objective optimization design of the $\underline{P}$UU-2$\underline{P}$R(R$\underline{P}$RR)S parallel mechanism.

5.1. Problem statement of multi-objective optimization

5.1.1. Performance indexes for optimization

For the proposed parallel mechanism, the optimization design would focus on working space, mechanism volume, and mechanism dexterity. Therefore, the following indicators are established based on the dimensionless principle.

Workspace volume ratio. The workspace volume ratio of this mechanism is defined as

$$\lambda_1 = \frac{V_{cw}}{V_{ow}} \tag{35}$$

where V_{ow} and V_{cw} represent the workspace of the mechanism before and after optimization, respectively. And, $\lambda_1 \geq 1$ means that the optimized workspace volume is larger than the original workspace volume.

Compactness. The compactness of this mechanism is defined as

$$\lambda_2 = \frac{V_{cm}}{V_{om}} \tag{36}$$

where V_{om} and V_{cm} represent the mechanism volume obtained before and after optimization, respectively.

Average dexterity ratio. The workspace of the mechanism is discretized into n points. Then the average dexterity is defined as

$$\bar{\kappa} = \frac{\sum_{i=1}^{n} \kappa_i}{n} \tag{37}$$

where $\bar{\kappa}$ is the average dexterity, and κ_i represents the dexterity of the i-th point.

Then, the average dexterity ratio of this mechanism is expressed as

$$\lambda_3 = \frac{\overline{\kappa_c}}{\overline{\kappa_o}} \tag{38}$$

where $\overline{\kappa_c}$ represents the optimized average dexterity, and $\overline{\kappa_o}$ means the average dexterity calculated by the initial structural parameters.

5.1.2. Constraints for optimal design

The main purpose of optimization design is to determine each rod length of the proposed $\underline{P}$UU-2$\underline{P}$R(R$\underline{P}$RR)S parallel mechanism. Here, it is notable that the sub-closed-loop (i.e. R$\underline{P}$RR) in the double-driven branch chain is treated as a rotation driver, and main lengths of the sub-closed-loop can be derived according to the angle range of the actuated revolute joint, that is, ϕ_i. Therefore, for simplicity, the position of E_i and D_i ($i = 1, 2$) is regarded as fixed. In other words, l_4 and l_5 are set to fixed values, that is, $l_4 = 200$ mm, $l_5 = 400$ mm. As the constraints, the design variables and their value ranges are shown in Table II.

5.1.3. Objective function

From the perspective of kinematic performance and economy, the objective of the optimal design is to obtain a parallel mechanism with large workspace, high compactness, and high dexterity. According to the above-defined performance indices, the larger the index λ_1 is, the larger the workspace of the parallel mechanism will be. The smaller the index λ_2 is, the better the compactness of the parallel mechanism is.

Table II. *Design variables and value range of the mechanism.*

Optimization parameters	Value range
l_1 (mm)	800∼1200
l_2 (mm)	320∼640
l_3 (mm)	480∼960
b (mm)	80∼320

And the larger the index λ_3 is, the better the dexterity of the parallel mechanism will be. Therefore, for consistency, the objective function of the multi-objective optimization problem can be defined as

$$f(X) = \max(f_1, f_2, f_3) = \max\left(\lambda_1, \frac{1}{\lambda_2}, \lambda_3\right) \tag{39}$$

where X is the vector composed of design variables.

5.2. Optimization method

Pareto optimization is a widely applied method of multi-objective optimization, and the set of all optimal solutions produced by Pareto optimization is called the Pareto front. All solutions on the Pareto front can be treated as equally good [49]. However, how to select the final optimization solution on the Pareto front will be a difficult problem. Generally, the performance graph produced by the Pareto front is utilized to select the final optimization result [50]. The performance graph graphically presents the relation between design variables and the performance indices. And for the optimization design with two objective functions, the Pareto front is a curve. However, for the optimization design with more than two objective functions, the Pareto front is usually a hypersurface, so its performance graph cannot be visually displayed [51].

The traditional Pareto optimization method directly obtains the Pareto front which contains all the indexes, but it cannot be displayed intuitively by the graph. To solve this problem, this paper proposed to convert the traditional Pareto optimization problem with multiple objectives into a stage-by-stage Pareto optimization problem, as shown in Fig. 11. The stage-by-stage Pareto optimization only should determine the priority of each optimization index according to the design requirements. The Pareto front between two indexes is obtained at each stage and the optimized space can be reduced stage by stage.

For clearly, main steps of the proposed stage-by-stage Pareto optimization are presented as follows.

Step 1. After the priority of optimization indexes is determined, single-objective optimization is carried out with λ_1 to determine the upper limit of f_1.

Step 2. Pareto front of f_1 and f_2 is obtained by the first stage Pareto optimization. This determines the range of f_2 in the second stage Pareto optimization.

Step 3. According to the step 2, Pareto optimization of the following stage is carried out, until the Pareto front of f_{n-1} and f_n is obtained, where n is the number of optimization indexes.

From Fig. 11, the final optimization result can be selected on the Pareto front of the final stage. The specific calculation process will be given in the next section with a numerical simulation.

5.3. Final optimized result using stage-by-stage Pareto

In order to verify the proposed multi-objective optimization method, the $\underline{P}$UU-2$\underline{P}$R(R$\underline{P}$RR)S parallel mechanism is taken as an example.
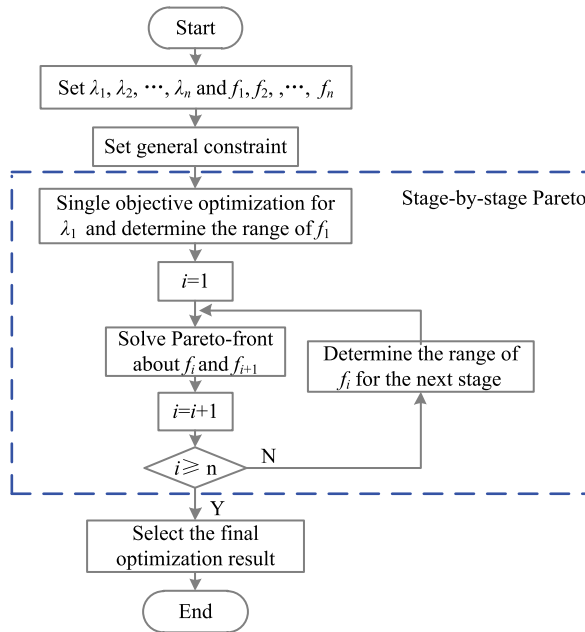
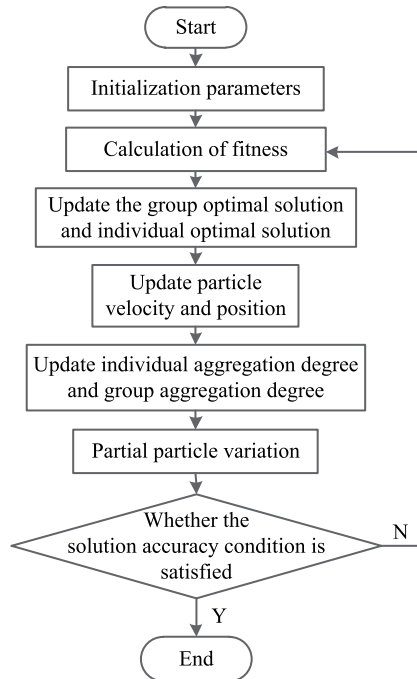**Figure 11.** *Flowchart of multi-objective optimization.*

Figure 12. *Flowchart of particle swarm optimization algorithm.*

According to the flowchart of multi-objective optimization as shown in Fig. 11, a single objective algorithm with f_1 should be conducted first. Here, the PSO is applied, and the corresponding flowchart is shown in Fig. 12. It is notable that different from the traditional PSO algorithm, the concept of particle aggregation degree [52] is introduced to avoid the local optimal solution. Figure 13 shows the change
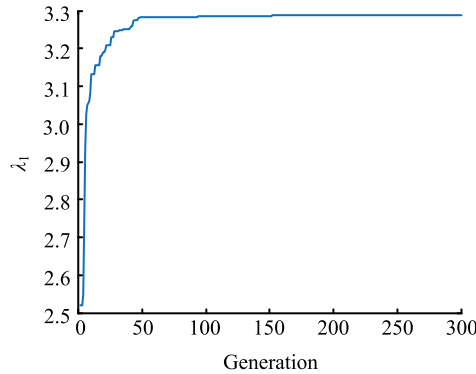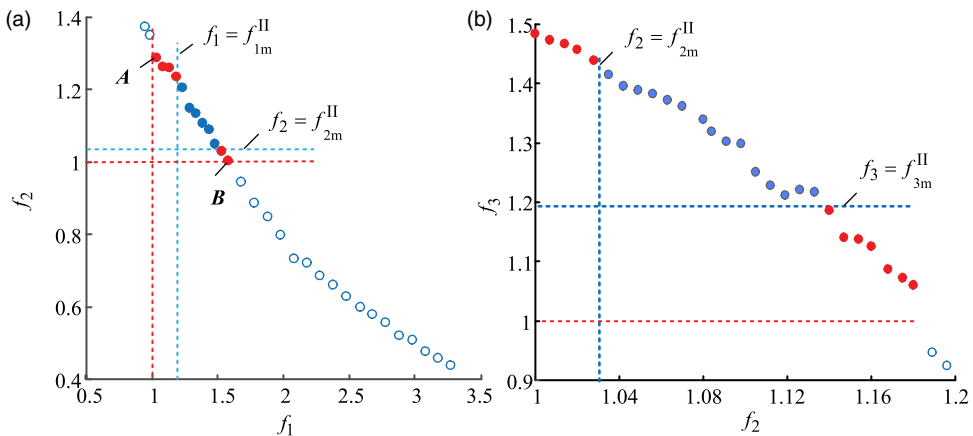
Figure 13. *The optimization results of λ_1.*

Figure 14. *The Pareto front of stage-by-stage Pareto. (a) The first stage. (b) The second stage.*

law of λ_1, and the value of λ_1 has converged to the optimal solution after 300 iterations. The maximum value of λ_1 is 3.28. It is taken as the upper limit of f_1 in the first stage Pareto optimization.

The stage-by-stage Pareto is also optimized using PSO. Figure 14(a) shows the Pareto front of first stage. The intersection of $f_1 \geq 1$ and $f_2 \geq 1$ on the Pareto front (i.e. the set of solid points in Fig. 14(a)) is the region where both objectives are optimized. Here, points $A = \begin{bmatrix} f_{1m}^I & f_{2M}^I \end{bmatrix}$ and $B = \begin{bmatrix} f_{1M}^I & f_{2m}^I \end{bmatrix}$ are two boundary points in this region as shown in Fig. 14(a).

In order to further reduce interval of feasible solutions, the minimum values of f_1 and f_2 that meet the optimization requirements can be set. The setting principle can be expressed as

$$f_{im}^{II} = f_{im}^I + \varepsilon_i \left(f_{iM}^I - f_{im}^I \right) \ (i = 1, 2, 3) \tag{40}$$

where ε_i is the optimized proportion of the i-th index. It is set according to the optimization requirements. The range of ε_i is $0 \leq \varepsilon_i \leq 1$. And in this example, the values of ε_1 and ε_2 are, respectively, set to 0.3 and 0.1, then f_{1m}^{II} and f_{2m}^{II} can be obtained. The range of the next stage of Pareto optimization is determined by the maximum and minimum values of f_2 in the intersection of $f_1 \geq f_{1m}^{II}$ and $f_2 \geq f_{2m}^{II}$ (i.e. the blue solid dot area in Fig. 14(a)).

On the premise that $f_1 \geq f_{1m}^{II}$, the Pareto front of the second stage can be obtained, as shown in Fig. 14(b). The Pareto front of f_2 and f_3 is reduced in the same way. f_{3m}^{II} can be calculated by setting $\varepsilon_3 = 0.3$. The intersection of $f_2 \geq f_{2m}^{II}$ and $f_3 \geq f_{3m}^{II}$ is chosen as the optimal solution set (i.e. the blue solid dot area in Fig. 14(b)).

Table III. *Parameters and performance indices of the final solution.*

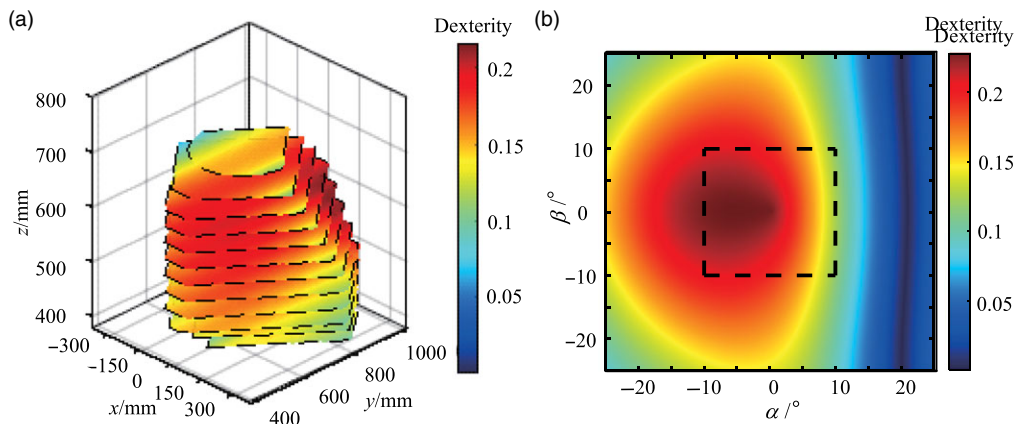| l_1 (mm)	l_2 (mm)	l_3 (mm)	b (mm)	λ_1	λ_2	λ_3
753.76	400.11	617.24	125.20	1.25	0.93	1.36

Figure 15. *Distribution map of optimized dexterity. (a) The distribution of the optimized dexterity in position space. (b) The distribution of the optimized dexterity in posture space.*

All the points in the optimal solution set meet the requirements of the optimal design. In order to select the final solution, ref. [19] proposed to establish a comprehensive performance index. In other words, the final optimization result can be selected by normalizing the performance index. Each performance index can be specified as

$$f_i^N = \frac{f_i - f_{im}}{f_{iM} - f_{im}} (i = 1, 2, 3) \tag{41}$$

where f_i^N is the established normalized performance index. f_{iM} and f_{im} are, respectively, the maximum and minimum values of the i-th objective function on the Pareto front after reduction in Fig. 14(b).

$$f = f_2^N + f_3^N \tag{42}$$

The higher the value of f is, the better the comprehensive performance of the mechanism is. Therefore, the solution with the best comprehensive performance in the optimal solution set is chosen as the optimal solution. Its structural parameters and corresponding indexes are shown in Table III.

Based on the optimized structural parameters, the optimal mechanism is obtained. The kinematic performance of the mechanism is improved. Workspace volume is increased by 25%, average dexterity is increased by 36%, and the volume of the mechanism is reduced by 7%.

Figure 15 shows the distribution map of the optimized dexterity. The dexterity is more evenly distributed compared to Fig. 9(a) in the same posture, and the maximum dexterity has been improved from 0.165 to 0.206 in the position workspace. Figure 15(b) shows dexterity of O_2^{dM} in posture workspace. Compared with Fig. 9(b), the distribution trend of dexterity does not change, but its maximum dexterity is improved from 0.169 to 0.220.

6. Conclusions

This paper focuses on the design and multi-objective optimization of a 5-DOF double-driven parallel mechanism. The main contributions are (1) a novel PUU-2PR(RPRR)S parallel mechanism with two double-driven chains is proposed. This 5-DOF parallel mechanism has less branch chains (i.e. three branch chains), reducing interference between branch chains. (2) A multi-objective optimization method

based on modified stage-by-stage Pareto is presented to improve multiple kinematics indexes. The proposed stage-by-stage Pareto can achieve intuitive selection of optimization results, reducing the difficulty of selecting final optimization result from the Pareto front. Conclusions of this paper can be drawn as follows.

Firstly, based on the idea of double-driven chains, the novel PUU-2PR(RPRR)S mechanism is proposed. On the premise of guaranteeing the number of DOF, the number of branch chains is reduced, simplifying mechanism's structure and reducing interference between branch chains. The DOF of this mechanism is analyzed by using screw theory, which shows that the proposed mechanism has five independent DOFs and a parasitic motion. Secondly, according to the geometric characteristics of this mechanism, the analytic form of inverse kinematics solution is derived. Then the 5×5 homogeneous Jacobian matrix is obtained by transforming actuator velocities into linear velocities at three points on the moving platform. Furthermore, kinematics characters of the mechanism are analyzed. The proposed mechanism has a continuous and regular workspace. Due to less number of branch chains, the mechanism has the advantages of small size, better economy, and higher compactness. And it has high dexterity in both posture space and position space. Finally, a modified stage-by-stage Pareto optimization method is proposed to solve the multi-objective optimization problem of the parallel mechanism. As the main improvement, the multi-objective optimization of three or more objectives is transformed into a stage-by-stage Pareto optimization method with only two objectives in each stage. Therefore, the optimization range of each objective can be intuitively selected in the form of performance graph, thus reducing the difficulty of selecting the final optimization results from the Pareto front. After the optimization, optimal structural parameters of the mechanism are obtained. The volume of working space is increased by 25%, average dexterity increased by 36%, and volume of the mechanism is reduced by 7%. These results also prove the effectiveness of the proposed stage-by-stage Pareto optimization method.

In order to further promote the practical engineering application of this proposed novel 5-DOF parallel mechanism as a machine tool, stiffness modeling and analysis will be focused in our future work. Multi-objective optimum design also will be systematically studied by considering both kinematic and stiffness performance indexes.

References

[1] M. Wu, Y. Zhang, X. Yue, D. Lv, M. Chen, X. Wang and J. Zhang, "Optimal design of an asymmetrical parallel mechanism," *Proc. Inst. Mech. Part C: J. Mech. Eng. Sci.* **235**(23), 6922–6939 (2021).

[2] P. Yan, H. Huang, B. Li and D. Zhou, "A 5-DOF redundantly actuated parallel mechanism for large tilting five-face machining," *Mech. Mach. Theory* **172**, 104785 (2022).

[3] M. Wu, X. Yue, W. Chen, Q. Nie and Y. Zhang, "Accuracy analysis and synthesis of asymmetric parallel mechanism based on Sobol-QMC," *Proc. Inst. Mech. Part C: J. Mech. Eng. Sci.* **234**(21), 4200–4214 (2020).

[4] J. Lacombe and C. Gosselin, "Singularity analysis of a kinematically redundant (6+2)-DOF parallel mechanism for zero-torsion configurations," *Mech. Mach. Theory* **170**, 104682 (2022).

[5] Q. Zou, D. Zhang, X. Luo, G. Huang, L. Li and H. Zhang, "Enumeration and optimum design of a class of translational parallel mechanisms with prismatic and parallelogram joints," *Mech. Mach. Theory* **150**, 1–15 (2020).

[6] M. K. Karnam, A. Baskar, R. A. Srivatsan and S. Bandyopadhyay, "Computation of the safe working zones of planar and spatial parallel manipulators," *Robotica* **38**(5), 861–885 (2020).

[7] P. Laryushkin, A. Antonov, A. Fomin and T. Essomba, "Velocity and singularity analysis of a 5-DOF (3T2R) Parallel-Serial (Hybrid) manipulator," *Machines* **10**(4), 276 (2022).

[8] J. Li, F. Ye, N. Shen, Z. Wang and L. Geng, "Dimensional synthesis of a 5-DOF hybrid robot," *Mech. Mach. Theory* **150**, 103865 (2020).

[9] Y. Wang, Y. Chen and R. Liu, "Aircraft image recognition network based on hybrid attention mechanism," *Comput. Intell. Neurosci.* **2022**, 4189500 (2022).

[10] X. Zhao, T. Zhao, X. Xu, H. Bian and S. Ding, "Kinematic analysis and dimensional synthesis of a three-degrees-of-freedom hybrid-drive parallel mechanism," *Proc. Inst. Mech. Part C: J. Mech. Eng. Sci.* **233**(8), 2728–2752 (2018).

[11] Y. Lu, P. Wang, S. Zhao, B. Hu, J. Han and C. Sui, "Kinematics and statics analysis of a novel 5-DoF parallel manipulator with two composite rotational/linear active legs," *Rob. Comput. Integr. Manuf.* **30**(1), 25–33 (2014).

[12] X. Zhao, T. Zhao, C. Wang, X. Tian and Y. Chen, "Type synthesis and analysis of parallel mechanisms with sub-closed-loops," *Mech. Mach. Theory* **120**, 140–165 (2018).

[13] S. Louis and G. Clement, "Exploiting the kinematic redundancy of a (6+3) degrees-of-freedom parallel mechanism," *J. Mech. Rob.* **11**(2), 021005 (2019).

[14] K. Wen and C. Gosselin, "Exploiting redundancies for workspace enlargement and joint trajectory optimisation of a kinematically redundant hybrid parallel robot," *ASME J. Mech. Rob.* **13**(4), 040905 (2021).

[15] H. Ren, Q. Li, B. Liu and Z. Dou, "Design and optimization of an elastic linkage quadruped robot based on workspace and tracking error," *Proc. Inst. Mech. Part C: J. Mech. Eng. Sci.* **232**(22), 4152–4166 (2018).

[16] K. J. Shibu, K. Shankar, C. K. Babu and G. K. Degaonkar, "Multi-objective optimization of a maneuvering small aircraft turbine engine rotor system," *J. Intell. Rob. Syst.* **103**(4), 1–14 (2021).

[17] E. Burkus, A. Odry, J. Awrejcewicz, I. Kecskes and P. Odry, "Mechanical design and a novel structural optimization approach for hexapod walking robots," *Machines* **10**(6), 466 (2022).

[18] C. Alessandro and S. Rosario, "Elastodynamic optimization of a 3T1R parallel manipulator," *Mech. Mach. Theory* **73**(73), 184–196 (2014).

[19] N. Luan, H. Zhang, H. Gui, S. Zhang, Y. Lin and J. Wu, "Placement and motion optimization of redundant maxillofacial surgical robot with new dexterity measure," *Int. J. Robot. Autom.* **31**(2), 118–127 (2016).

[20] J. Wu, X. Wang, B. Zhang and T. Huang, "Multi-objective optimal design of a novel 6-DOF spray-painting robot," *Robotica* **39**(12), 2268–2282 (2021).

[21] G. Huang, S. Guo, D. Zhang, H. Qu and H. Tang, "Kinematic analysis and multi-objective optimization of a new reconfigurable parallel mechanism with high stiffness," *Robotica* **36**(2), 187–203 (2017).

[22] Y. Xu, L. Cheng, J. Yang, Y. Ji, H. Wang, H. Sun, C. Liu and B. Zhang, "Cartesian space track planning for welding robot with inverse solution multi-objective optimization," *Meas Control-UK* **55**(7-8), 583–594 (2022).

[23] A. Rosyid, B. El-Khasawneh and A. Alazzam, "Genetic and hybrid algorithms for optimization of non-singular 3PRR planar parallel kinematics mechanism for machining application," *Robotica* **36**(6), 839–864 (2018).

[24] C. Li, N. Wang, K. Chen and X. Zhang, "Prescribed flexible orientation workspace and performance comparison of non-redundant 3-DOF planar parallel mechanisms," *Mech. Mach. Theory* **168**, 104602 (2022).

[25] G. Zhao, M. Zhu and M. D. Hayes, "Pareto optimal multirobot motion planning," *IEEE Trans. Autom. Control* **66**(9), 3984–3999 (2021).

[26] A. Guigue, M. Ahmadi, R. Langlois and M. D. Hayes, "Pareto Optimality and multiobjective trajectory planning for a 7-DOF redundant manipulator," *IEEE Trans. Rob.* **26**(6), 1094–1099 (2010).

[27] S. Herrero, C. Pinto, M. Diez and A. Zubizarreta, "Optimization of the 2PRU-1PRS parallel manipulator based on workspace and power consumption criteria," *Appl. Sci.* **11**(17), 7770 (2021).

[28] Y. Sato, K. Izui, T. Yamada and S. Nishiwaki, "Pareto frontier exploration in multiobjective topology optimization using adaptive weighting and point selection schemes," *Struct. Multidiplinary Optim.* **55**(2), 409–422 (2017).

[29] M. Russo, S. Herrero, O. Altuzarra and M. Ceccarelli, "Kinematic analysis and multi-objective optimization of a 3-UPR parallel mechanism for a robotic leg," *Mech. Mach. Theory* **120**, 192–202 (2018).

[30] Y. Qi, T. Sun and Y. Song, "Multi-objective optimization of parallel tracking mechanism considering parameter uncertainty," *ASME J. Mech. Rob.* **10**(4), 041006 (2018).

[31] M. Elsisy, M. Sayed, Y. Abo-Elnaga and Y. Elsayed, "Engineering physics and mathematics a novel algorithm for generating Pareto frontier of bi-level multi-objective rough nonlinear programming problem," *Ain Shams Eng. J.* **12**(2), 2125–2133 (2021).

[32] G. Wang, Q. Hu, C. Xu, B. Zhao and X. Su, "Analysis and Pareto frontier based tradeoff design of an integrated magnetic structure for a CLLC resonant converter," *Energies* **14**(6), 1756 (2021).

[33] T. Sun and B. Lian, "Stiffness and mass optimization of parallel kinematic machine," *Mech. Mach. Theory* **120**, 73–88 (2018).

[34] B. Bounab, "Multi-objective optimal design based kineto-elastostatic performance for the DELTA parallel mechanism," *Robotica* **34**(2), 258–273 (2016).

[35] S. Farooq, A. Baqai and M. Shah, "Optimal design of tricept parallel manipulator with particle swarm optimization using performance parameters," *J. Eng. Res.* **9**(2), 378–395 (2021).

[36] Y. Yun and Y. Li, "Optimal design of a 3-PUPU parallel robot with compliant hinges for micromanipulation in a cubic workspace," *Rob. Comput. Integr. Manuf.* **27**(6), 977–985 (2011).

[37] H. Wang, L. Zhang, G. Chen and S. Huang, "Parameter optimization of heavy-load parallel manipulator by introducing stiffness distribution evaluation index," *Mech. Mach. Theory* **108**, 244–259 (2017).

[38] A. Ruiz, F. J. Campa, C. Roldan-Paraponiaris, O. Altuzarra and C. Pinto, "Experimental validation of the kinematic design of 3-PRS compliant parallel mechanisms," *Mechatronics* **39**, 77–88 (2016).

[39] X. Chen, X. Liu, F. Xie and T. Sun, "A comparison study on motion/Force transmissibility of two typical 3-DOF parallel manipulators: The Sprint Z3 and A3 tool heads," *Int J. Adv. Rob. Syst.* **11**(1), 1–10 (2014).

[40] X. Kang, H. Feng, J. S. Dai and H. Yu, "High-order based revelation of bifurcation of novel Schatz-inspired metamorphic mechanisms using screw theory," *Mech. Mach. Theory* **152**, 103931 (2020).

[41] Q. Li, Z. Chen, Q. Chen, C. Wu and X. Hu, "Parasitic motion comparison of 3-PRS parallel mechanism with different limb arrangements," *Rob. Comput. Integr. Manuf.* **27**(2), 389–396 (2011).

[42] Z. Chen, X. Chen, M. Gao, C. Zhao, K. Zhao and Y. Li, "Motion characteristics analysis of a novel spherical two-degree-of-freedom parallel mechanism," *Chin. J. Mech. Eng.* **35**(1), 1–9 (2022).

[43] S. Khan, K. Andersson and J. Wikander, "Jacobian matrix Normalization - a comparison of different approaches in the context of multi-objective optimization of 6-DOF haptic devices," *J. Intell. Rob. Syst.* **79**(1), 87–100 (2015).

[44] L. Nurahmi and S. Caro, "Dimensionally homogeneous Jacobian and condition number," *Appl. Mech. Mater.* **836**, 42–47 (2015).

[45] G. Cui, J. Liu, Z. Hu, Y. Zhang and H. Hou, "Performance analysis and optimization of a rigid-flexible parallel manipulator," *Proc. Inst. Mech. Part C: J. Mech. Eng. Sci.* **234**(23), 4620–4635 (2020).

[46] Y. Guan, H. Zhang, X. Zhang and Z. Guan, "Workspace generation for multifingered manipulation," *Adv. Rob.* **25**(18), 2293–2317 (2011).

[47] C. Lin, P. Jo and C. Tseng, "New compliance-mechanism design for small companion robots," *J. Intell. Rob. Syst.* **64**(3-4), 585–601 (2011).

[48] L. Li, Y. Fang, J. Yao and L. Wang, "Type synthesis of a family of novel parallel leg mechanisms driven by a 3-DOF drive system," *Mech. Mach. Theory* **167**, 104572 (2022).

[49] C. S. Miranda and F. Zuben, "Necessary and sufficient conditions for surrogate functions of Pareto frontiers and their synthesis using Gaussian processes," *IEEE Trans. Evol. Comput.* **21**(1), 1–13 (2017).

[50] J. Wu, L. Wang and Z. You, "A new method for optimum design of parallel manipulator based on kinematics and dynamics," *Nonlinear Dyn.* **61**(4), 717–727 (2010).

[51] M. C. De Oliveira, M. R. Delgado and A. Britto, "A hybrid greedy indicator- and Pareto-based many-objective evolutionary algorithm," *Int. J. Appl. Intell.* **51**(7), 4330–4352 (2021).

[52] A. Rios, E. E. Hernandez and S. I. Valdez, "A two-stage mono- and multi-objective method for the optimization of general UPS parallel manipulators," *Mathematics* **9**(5), 1–20 (2021).